Phase diagram of a distorted kagome antiferromagnet and application to Y-kapellasite – Supplementary Information –

Max Hering,[1,2] Francesco Ferrari,[3] Aleksandar Razpopov,[3] Igor I. Mazin,[4] Roser Valentí,[3] Harald O. Jeschke,[5] and Johannes Reuther[1,2]

[1] *Helmholtz-Zentrum Berlin für Materialien und Energie, Hahn-Meitner Platz 1, 14109 Berlin, Germany*
[2] *Dahlem Center for Complex Quantum Systems and Fachbereich Physik, Freie Universität Berlin, 14195 Berlin, Germany*
[3] *Institute for Theoretical Physics, Goethe University Frankfurt, Max-von-Laue-Straße 1, 60438 Frankfurt am Main, Germany*
[4] *Department of Physics and Astronomy, and Quantum Science and Engineering Center, George Mason University, Fairfax, VA 22030, USA*
[5] *Research Institute for Interdisciplinary Science, Okayama University, Okayama 700-8530, Japan*

(Dated: November 29, 2021)

Supplementary Note 1. Finite-size clusters

Most of the numerical calculations of this work are performed on finite-size clusters with periodic boundary conditions. We consider two classes of fully symmetric finite-size clusters, *type-I* and *type-II*, which are defined by two different choices for the boundary conditions. *Type-I* clusters are constructed by imposing periodic boundary conditions along the vectors $\vec{T}_1 = L\vec{a}_1$ and $\vec{T}_2 = L\vec{a}_2$, for a total of $N = 9L^2$ sites. Only the *Type-I* clusters in which L is a multiple of 3 can accommodate the $\vec{Q} = (1/3, 1/3)$ magnetic order. For *type-II* clusters, instead, we take periodic boundary conditions along $\vec{T}_1 = L(\vec{a}_1 - \vec{a}_2)$ and $\vec{T}_2 = L(2\vec{a}_1 + \vec{a}_2)$, which are parallel to the axes of the ideal (undistorted) kagome lattice. *Type-II* clusters contain $N = 27L^2$ sites, and they can always accommodate the $\vec{Q} = (1/3, 1/3)$ order, regardless of the value of L. In Supplementary Fig. 1 we show the small finite-size clusters employed for the iterative minimization calculations, i.e. the $L = 2$ *type-I* cluster with $N = 36$ sites and the $L = 1$ *type-II* cluster with $N = 27$ sites.

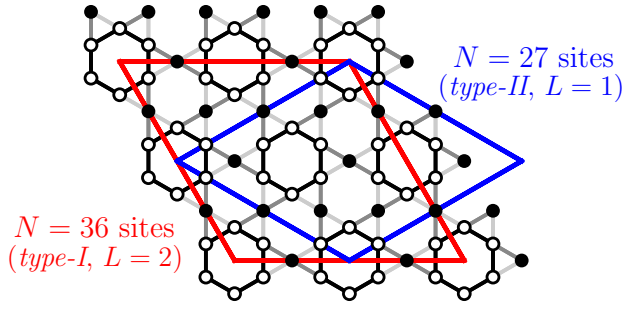

Supplementary Figure 1. Finite-size clusters used for iterative minimization, classical Monte Carlo, and variational Monte Carlo calculations.

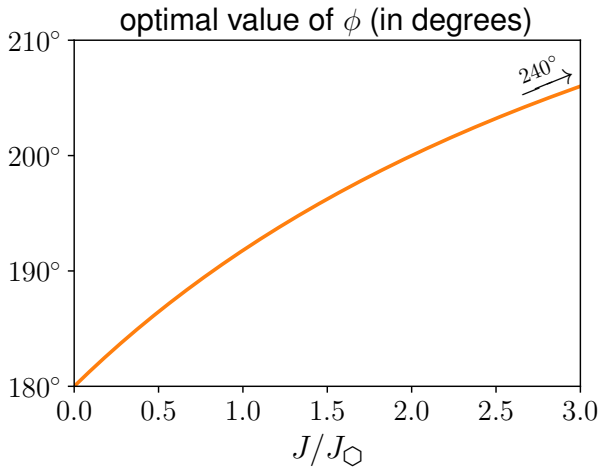

Supplementary Figure 2. Optimal value of the angle ϕ for the $\vec{Q} = (1/3, 1/3)$ magnetic order of Fig. 1c of the main text as a function of the $J/J_\bigcirc$ ratio ($J' = 0$).

Supplementary Note 2. More on the $\vec{Q} = (1/3, 1/3)$ ordered phase

In the limit $J' = 0$, the energy of the classical spin configuration is given by Eq. (7) of the main text. The optimal value of ϕ is obtained by the minimization of this energy and its dependency on the ratio $J/J_\bigcirc$ is shown in Supplementary Fig. 2.

Further insight is gained by looking at two extreme limits of the ratio $J/J_\bigcirc$. When $J \ll J_\bigcirc$ (*strong hexagons* limit), the angle $\phi \to \pi$, namely the spins of A sites form an antiferromagnetic pattern around the $J_\bigcirc$-hexagons. On the other hand, in the opposite limit, $J \gg J_\bigcirc$ (*trimer* limit), the angle $\phi \to 4\pi/3$ and the spins of sublattice B are antiferromagnetically aligned with respect to the two nearest-neighboring A sites, thus forming antiferromagnetic trimers as shown in the main text, Fig. 1d. Considering the trimers as single effective spins, we note that they form a kagome lattice and they interact through an effective antiferromagnetic coupling (each trimer is connected

name	d_{Cu-Cu} (Å)	assignment
$J_1 \equiv J'$	3.24978	inplane 1nn
$J_2 \equiv J_{\hexagon}$	3.36832	inplane 1nn
$J_3 \equiv J$	3.37619	inplane 1nn
J_4	5.67876	interlayer
J_5	5.70735	inplane 2nn
J_6	5.76750	inplane 2nn
J_8	5.86065	interlayer

U (eV)	J_1 (K)	J_2 (K)	J_3 (K)	J_4 (K)	J_5 (K)	J_6 (K)	J_8 (K)	$T_{\rm CW}$ (K)
4	11.3(9)	161.1(6)	189.1(9)	-0.5(1.0)	4.2(6)	0.5(6)	2.0(9)	-122
4.5	10.2(7)	149.3(5)	174.0(7)	-0.9(8)	3.8(5)	0.5(5)	1.4(7)	-113
5	9.1(6)	138.7(4)	160.3(6)	-1.2(7)	3.4(4)	0.4(4)	0.9(6)	-104
5.23	**8.7(6)**	**134.2(4)**	**154.4(6)**	**-1.3(7)**	**3.2(4)**	**0.4(4)**	**0.7(6)**	**-100**
5.5	8.2(5)	129.1(3)	147.8(5)	-1.4(5)	3.0(3)	0.4(3)	0.5(5)	-96
6	7.4(4)	120.2(3)	136.4(4)	-1.4(5)	2.7(3)	0.3(3)	0.2(4)	-89
6.5	6.6(3)	112.0(2)	125.8(3)	-1.5(4)	2.3(2)	0.3(2)	0.0(3)	-82
7	5.9(3)	104.4(2)	116.0(3)	-1.4(3)	2.0(2)	0.2(2)	-0.2(3)	-76
7.5	5.2(2)	97.2(2)	106.9(2)	-1.4(3)	1.7(2)	0.2(2)	-0.3(2)	-70
8	4.5(2)	90.5(1)	98.5(2)	-1.3(2)	1.5(2)	0.1(2)	-0.4(2)	-65

Supplementary Table 1. Exchange couplings of $Y_3Cu_9(OH)_{19}Cl_8$ ($S_{\rm XRD}$ structure), calculated within GGA+U and $6\times6\times6$ k points. The experimental value $T_{\rm CW} = -100$ K of the Curie Weiss temperature is matched by the line in bold face. Statistical errors are indicated.

name	d_{Cu-Cu} (Å)	assignment
$J_1 \equiv J'$	3.25310	inplane 1nn
$J_2 \equiv J$	3.36068	inplane 1nn
$J_3 \equiv J_{\hexagon}$	3.37591	inplane 1nn
J_4	5.68423	interplane 1nn
J_5	5.68831	inplane 2nn
J_6	5.76630	inplane 2nn
J_7	5.77832	inplane 2nn

U (eV)	J_1 (K)	J_2 (K)	J_3 (K)	J_4 (K)	J_5 (K)	J_6 (K)	J_7 (K)	$T_{\rm CW}$ (K)
4	11.2(7)	151.4(8)	154.3(5)	-1.0(7)	5.7(5)	0.8(5)	3.3(7)	-108
4.46	**10.3(7)**	**139.8(8)**	**143.9(5)**	**-1.3(7)**	**5.2(5)**	**0.8(5)**	**2.6(7)**	**-100**
4.5	10.3(6)	138.8(7)	143.0(4)	-1.3(6)	5.2(4)	0.7(4)	2.6(6)	-99
5	9.4(5)	127.4(6)	132.7(3)	-1.5(5)	4.6(3)	0.6(3)	1.9(5)	-91
5.5	8.5(4)	117.1(5)	123.4(3)	-1.6(4)	4.1(3)	0.5(3)	1.4(4)	-84
6	7.7(3)	107.7(4)	114.9(2)	-1.6(3)	3.6(2)	0.5(2)	1.1(3)	-78
6.5	6.8(3)	99.1(3)	107.0(2)	-1.6(3)	3.2(2)	0.4(2)	0.7(3)	-72
7	6.1(2)	91.1(3)	99.6(2)	-1.5(2)	2.8(2)	0.3(2)	0.5(2)	-66
7.5	5.3(2)	83.8(2)	92.7(1)	-1.4(2)	2.4(2)	0.2(2)	0.3(2)	-61
8	4.5(2)	77.0(2)	86.3(1)	-1.3(2)	2.1(1)	0.2(1)	0.1(2)	-56

Supplementary Table 2. Exchange couplings of $Y_3Cu_9(OH)_{19}Cl_8$ ($S_{\rm ND}$ structure), calculated within GGA+U and $6\times6\times6$ k points. The experimental value $T_{\rm CW} = -100$ K of the Curie Weiss temperature is matched by the line in bold face. Statistical errors are indicated.

to four other trimers by a $J_{\hexagon}$ bond). In this limit, the $\vec{Q} = (1/3, 1/3)$ magnetic order of our model reduces to the $\sqrt{3}\times\sqrt{3}$ order [3] of the effective kagome lattice made by the antiferromagnetic trimers.

As discussed in the main text, the linear spin wave dispersion of the $\vec{Q} = (1/3, 1/3)$ order in the *strong hexagon* ($J \ll J_{\hexagon}$, Fig.3a) and *trimer* ($J \gg J_{\hexagon}$, Fig.3c) limits share similarities with those of the triangular lattice 120° order [1] and of the kagome lattice $\sqrt{3}\times\sqrt{3}$ order [3], respectively. In Supplementary Fig. 3 we show the linear spin wave dispersions for the latter two cases, for comparison.

Supplementary Note 3. More on the classical spin liquid phase

It is worth mentioning that the $J = J'$ line represents a special case within this region, where coplanar ground states with $\vec{L}_{\triangle} = 0$ can be analytically defined. Indeed, in this special limit, for each triangle we can write

$$\vec{L}_{\triangle} = J\vec{S}_b + \vec{S}_a + \vec{S}_{a'}, \tag{1}$$

where a and a' are two neighboring sites of sublattice A, b is a site of sublattice B and we have set $J_{\hexagon} = 1$ for

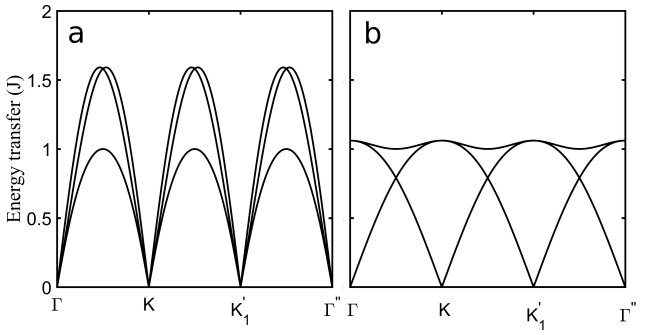

Supplementary Figure 3. Linear spin wave dispersions for **a** the 120° magnetic order in the antiferromagnetic Heisenberg model on the triangular lattice [1] and **b** the $\sqrt{3}\times\sqrt{3}$ order in the antiferromagnetic Heisenberg model on the kagome lattice [2]. We note that in the latter case the true ground state of the $S = 1/2$ system is not magnetically ordered. A zero-energy dispersionless mode is present in the linear spin-wave spectrum of the $\sqrt{3}\times\sqrt{3}$ order on the kagome lattice [2]. In both panels the spin wave energies are plotted along the $\Gamma - K - K_1' - \Gamma$ line (see Fig.1b of the main text).

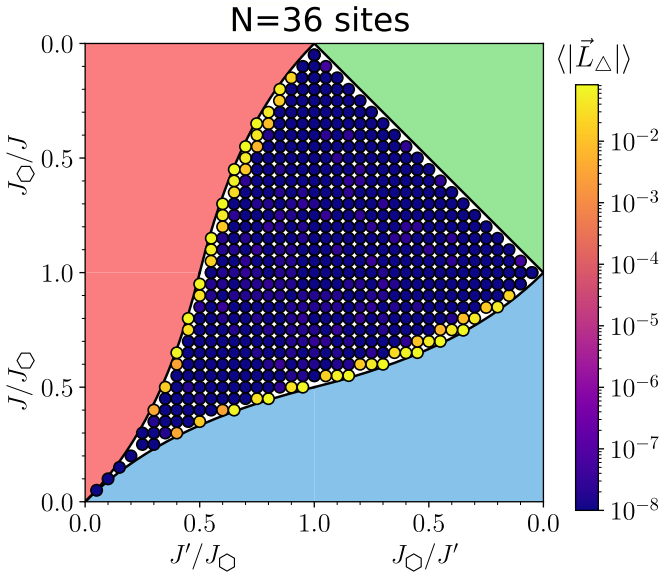

Supplementary Figure 4. Value of $\langle|\vec{L}_\triangle|\rangle$ (averaged over triangles) in the optimal classical ground state found by iterative minimization. The results are obtained in the classical spin liquid phase, on the $N = 36$ sites cluster sketched in Supplementary Fig. 1 (*type-I*, $L = 2$, see Supplementary Note 1 for details). Close to the inner boundaries of the spin-liquid phase, we find a number of points where the system is characterized by two distinct non-coplanar degenerate ground states with $\langle|\vec{L}_\triangle|\rangle > 0$. We note that the $N = 36$ sites cluster cannot accommodate the $\vec{Q} = (1/3, 1/3)$ order.

simplicity. Since this expression is valid for all triangles of the system, simple solutions with $\vec{L}_\triangle = 0$, $\forall\triangle$ can be found by focusing on a single unit cell. There, we can set, e.g., $S_b = (1, 0, 0)$ for all sites of sublattice B and we can choose an alternating pattern for the sites of sublattice A forming

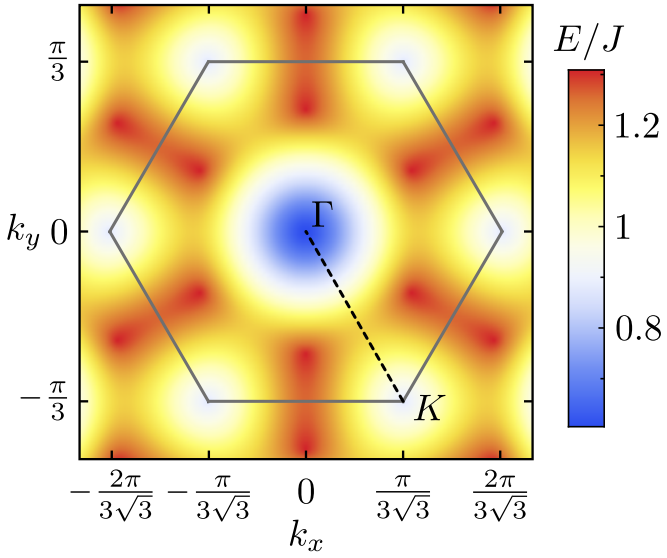

Supplementary Figure 5. Third band of the coupling matrix [see Eq. (2)] depicted in the first Brillouin zone (gray hexagon). Energies E are indicated relative to the bottom of the lowest band. The dashed line marks a valley in the band structure which may explain the system's unusual thermal fluctuations.

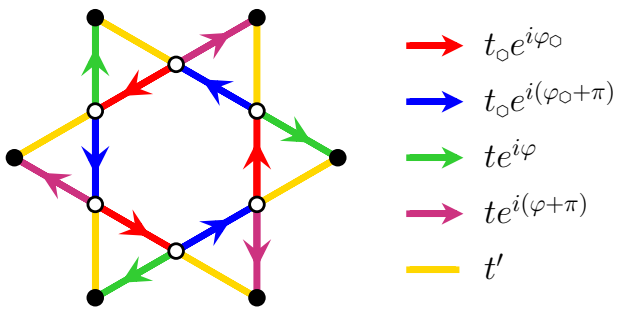

Supplementary Figure 6. Optimal hopping pattern of the best variational *Ansatz* [Eq. (5)] for the effective spin model of Y-Kapellasite. The empty (full) dots represent the sites of sublattice A (B). The arrows encode the convention for complex hoppings: $i \to j$ represents the hopping terms $t_{i,j}c^\dagger_{i,\sigma}c_{j,\sigma}$ ($\sigma = \uparrow, \downarrow$). A total of five real parameters is used to parametrize the hopping part of the variational *Ansatz* ($t_\bigcirc, t, t', \varphi_\bigcirc, \varphi$).

the $J_\bigcirc$-hexagons, where we have $S_a = (\cos(\theta), \sin(\theta), 0)$ for odd sites and $S_{a'} = (\cos(\theta), -\sin(\theta), 0)$ for even sites, with $\theta = \arccos(-J/2)$. The same analysis can be repeated for each unit cell separately and coplanar ground states can be constructed, as discussed also in Ref. [4], where the $J = J'$ model is investigated in connection to the physics of Volborthite. We note that this solution is connected to the $\vec{Q} = 0$ coplanar order, since for $J = J' = 2J_\bigcirc$ we get $\theta = \pi$, i.e. the spins inside the $J_\bigcirc$-hexagons are ferromagnetically arranged, and antiparallel to the spins of sublattice B.

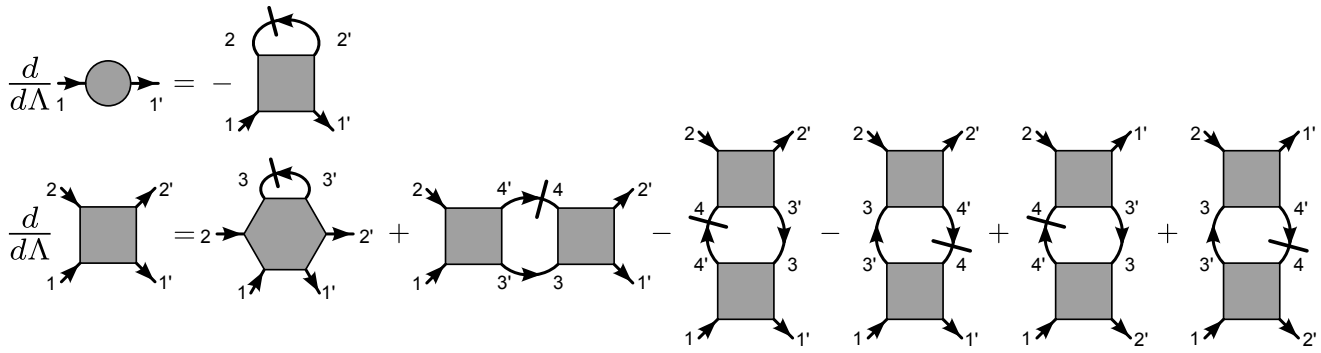

Supplementary Figure 7. Diagrammatic representation of the PFFRG flow equations for Σ^Λ (circle) and Γ^Λ (square). Slashed (bare) arrows depict the single-scale propagator S^Λ (dressed propagator G^Λ). Since the two-particle vertex couples to the three-particle vertex (hexagon), the flow equations are truncated at this level. External legs contain one full set of quantum numbers each and internal quantum numbers have to be summed up or integrated.

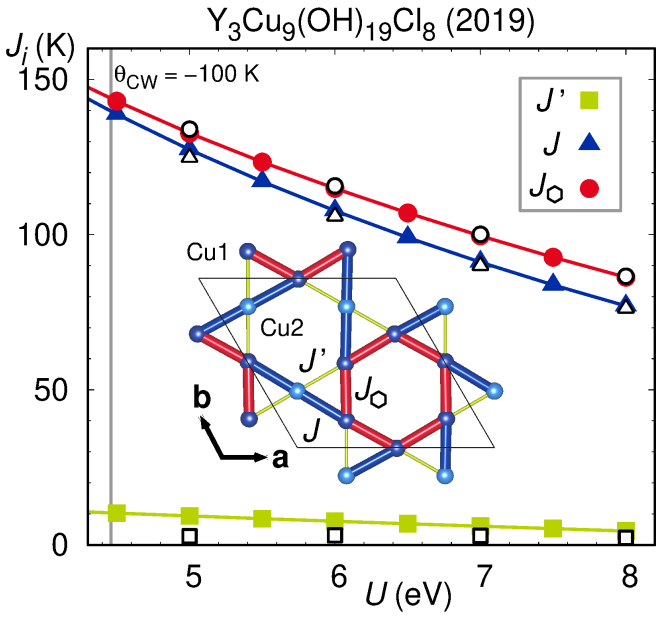

Supplementary Figure 8. Exchange couplings of $Y_3Cu_9(OH)_{19}Cl_8$ (S_{ND} structure) extracted with GGA+U at $J_H = 1$ eV as function of interaction strength U. Solid symbols: $P1$ cell, 7 couplings extracted. Empty symbols: $\sqrt{2} \times \sqrt{2} \times 1$ supercell, 24 couplings extracted.

name	d_{Cu-Cu} (Å)	J_i (K)	assignment
J_1	3.24978	8.4(9)	inplane 1nn Cu1-Cu2
J_2	3.36832	133.1(6)	inplane 1nn Cu1-Cu1
J_3	3.37619	152.0(9)	inplane 1nn Cu1-Cu2
J_4	5.67876	0.3(8)	interlayer
J_5	5.70735	1.0(5)	inplane 2nn Cu1-Cu1
J_6	5.76750	0.6(6)	inplane 2nn Cu2-Cu2
J_7	5.83040	3.0(5)	inplane 2nn Cu1-Cu1
J_8	5.86065	0.0(6)	interlayer
J_9	6.49956	-0.6(5)	inplane 3nn ($2J_1$, Cu1-Cu1)
J_{10}	6.51314	-0.5(6)	interlayer
J_{11}	6.57249	-0.5(5)	interlayer
J_{12}	6.61523	-1.7(7)	inplane 3nn (J_1+J_2, Cu1-Cu2)
J_{13}	6.62488	-0.3(7)	inplane 3nn (J_1,J_3 hex., Cu1-Cu2)
J_{14}	6.63443	-1.6(9)	interlayer
J_{15}	6.66444	0.2(7)	interlayer
J_{16}	6.69872	-0.2(5)	interlayer
J_{17}	6.72699	0.4(6)	interlayer
J_{18}	6.73343	1.2(5)	inplane 3nn (J_2 hex., Cu1-Cu1)
J_{19}	6.74065	0.2(8)	inplane 3nn (J_2+J_3, Cu1-Cu2)
J_{20}	6.75238	-0.1(6)	inplane 3nn ($2J_3$, Cu1-Cu1)
J_{21}	8.04603	0.7(8)	interlayer
J_{22}	8.09002	3.2(5)	interlayer
J_{23}	8.09791	0.4(7)	interlayer
J_{24}	8.14162	1.0(7)	interlayer

Supplementary Table 3. Exchange couplings of $Y_3Cu_9(OH)_{19}Cl_8$ (S_{XRD} structure), calculated within GGA+U and $4 \times 4 \times 4$ k points. The couplings are reported at $U = 5.28$ eV; this U value is obtained by demanding that the model matches the experimental Curie-Weiss temperature. Statistical errors are indicated.

Supplementary Note 4. Analytical approach to explain classical Monte Carlo data

In this Supplementary Note we discuss the origin of the unusual peak shift in the classical Monte Carlo data for the S_{XRD} structure as a function of temperature, as observed in Fig. 5 of the main text. A possible explanation for this behavior comes from the system's coupling matrix in momentum space

$$J_{\rho\sigma}(\vec{k}) = \sum_{\vec{r}_a - \vec{r}_b} e^{i\vec{k}(\vec{R}_a - \vec{R}_b)} J_{a\rho b\sigma} \ , \qquad (2)$$

which forms the basis for various analytical techniques for studying classical spin systems. Here, the sites i are characterized by the two indices a and ρ, specifying the unit cell and the sublattice of site i, respectively. Similarly, $j \to b, \sigma$ and $J_{ij} \to J_{a\rho b\sigma}$, yielding the 9×9 matrix $J_{\rho\sigma}(\vec{k})$. Furthermore, $\vec{R}_a$, $\vec{R}_b$ specify the positions of the unit cells a and b. Diagonalizing this matrix for the couplings of the S_{XRD} structure one finds that the third band (when counting from the lowest one) is in an energy range from $E \sim 0.6J$ to

$E \sim 1.3J$ relative to the bottom of the lowest band. This intermediate energy range roughly corresponds to the temperature regime at which the peak shift in Monte Carlo is observed, i.e., the third band can be expected to be connected to these unusual thermal fluctuations. Indeed, as shown in Supplementary Fig. 5 the third band exhibits a pronounced valley between the K and Γ points (dashed line in Supplementary Fig. 5) such that fluctuations preferably occur along this direction. Note that the magnetic band structure is defined in the first Brillouin zone such that all points Γ', Γ'' are folded back onto Γ and, equivalently, K_1', K_2', K_3' all map onto K.

Supplementary Note 5. Details on the variational Monte Carlo calculations

The variational Monte Carlo (VMC) calculations for the Hamiltonian of Y-kapellasite make use of Gutzwiller-projected fermionic wave functions as variational *Ansätze*. The definition of these states is based on the Abrikosov fermion representation of $S = 1/2$ spins,

$$\vec{S}_i = \frac{1}{2} \sum_{\alpha,\beta} c^\dagger_{i,\alpha} \vec{\sigma}_{\alpha,\beta} c_{i,\beta}. \tag{3}$$

Here $\vec{\sigma} = (\sigma_x, \sigma_y, \sigma_z)$ is a vector of Pauli matrices and $c_{i,\alpha}$ ($c^\dagger_{i,\alpha}$) are fermionic annihilation (creation) operators. Within this formalism, suitable variational states for spin systems can be constructed by applying the Gutzwiller projector, $\mathcal{P}_G = \sum_i (n_{i,\uparrow} - n_{i,\downarrow})^2$, to a fermionic wave function, e.g. a Slater determinant [5]. The Gutzwiller operator enforces the single occupation of each lattice site and projects the fermionic wave function onto the spin Hilbert space. In this work, we consider Gutzwiller-projected Jastrow-Slater variational *Ansätze* of the form

$$|\Psi_0\rangle = \mathcal{J}\mathcal{P}_G |\Phi_0\rangle. \tag{4}$$

Here, $|\Phi_0\rangle$ is the ground state of an auxiliary quadratic Hamiltonian of Abrikosov fermions, named $\mathcal{H}_0$, which includes first-neighbor hopping terms ($t_{i,j}$) and a site-dependent magnetic field of strength h:

$$\mathcal{H}_0 = \sum_{\langle i,j \rangle} \sum_\sigma t_{i,j} c^\dagger_{i,\sigma} c_{j,\sigma} + \text{h.c.} + h \sum_i \hat{n}^Q_i \cdot \vec{S}_i. \tag{5}$$

The local orientation of the magnetic field, given by the unit vector $\hat{n}^Q_i$, is chosen such that it induces the optimal single-$\vec{Q}$ classical order in the (S_x, S_y)-plane. Since we focus on the exchange couplings derived for the S_{XRD} structure of Y-kapellasite, our magnetic field corresponds to the best classical order with $\vec{Q} = (1/3, 1/3)$ periodicity. Non-trivial quantum fluctuations are introduced by the hopping terms $t_{i,j}$ of the auxiliary Hamiltonian $\mathcal{H}_0$, and by the application of a long-range spin-spin Jastrow

$$\mathcal{J} = \exp\left[\sum_{i,j} v(i,j) S^z_i S^z_j\right]. \tag{6}$$

on top of the Gutzwiller-projected fermionic state [see Eq. (4)]. The optimal parametrization of the hoppings, which yields the best variational energy for the exchange couplings of the S_{XRD} structure, is illustrated in Supplementary Fig. 6.

Supplementary Note 6. Additional DFT results

In this Supplementary Note we present the full set of Heisenberg exchange coupling constants up to n^{th} neighbors. These values were extracted from spin-polarized *ab initio* DFT calculations by making use of the total energy mapping method as explained in the main text. Supplementary Table 1 shows the results for the S_{XRD} structure (see Fig. 6 of the main text for the definition of $J_\bigcirc$, J and J') up to 8^{th} neighbors, and Supplementary Table 2 shows the results for the S_{ND} structure up to 7^{th} neighbors, where the definitions of $J_\bigcirc$, J and J' are indicated in Supplementary Fig. 8. As explained in the method section of the main text, we perform the energy mapping method by calculating far more total energies than would be minimally required to extract the exchange interactions; for example, for extracting 7 exchange interactions, we calculate 24 energies instead of the minimal number 8. Fitting the Hamiltonian using singular value decomposition yields a statistical error for the exchange couplings which is indicated in Tables 1 to 3. These errors give an indication of the uncertainty of the Hamiltonian parameters calculated for a particular crystal structure; however, the impact of the uncertainties in the crystal structure on the exchange couplings is not included.

In order to check the presence of possible long-ranged coupling constants, we also performed calculations for larger supercells of the S_{XRD} structure and extracted values of the exchange coupling constants up to 24^{th} neighbors, as shown in Table 3. This calculation is computationally very demanding and cannot be repeated for all structures and values of U. However, it is an important sanity check because it is the nature of the energy mapping method that a calculation with a small cell yielding few exchange interactions effectively provides information on each coupling with some average of unresolved longer range exchange couplings added to it. By resolving more couplings as shown in Supplementary Table 3, we have verified that there are no important long range exchange couplings that could have introduced errors into the couplings shown in Supplementary Tables 1 and 2 or that would significantly modify the magnetic properties. Comparing the coupling J_5 at $U = 5.23\,\text{eV}$ obtained in the smaller cell ($J_5 = 3.2(4)\,\text{K}$) to that obtained in the large supercell ($J_5 = 1.0(5)\,\text{K}$), we find that the larger value 3.2 K is not substantiated, and it is reasonable to focus all further analysis on the first three exchange couplings $J_\bigcirc$, J and J'.

Supplementary Note 7. Comparison of VMC and PFFRG results

While VMC and PFFRG both find magnetic long range order for Y-kapellasite, the small peak shift and the rather broad susceptibility profile in PFFRG are not seen in VMC, which detects sharp Bragg peaks at the ordering vectors (compare Fig. 7 and Fig.8 b of the main text). Given that the two techniques are conceptually very different and rely on different approximations, such discrepancies are not surprising. For example, detecting incommensurate magnetic order within VMC is a hard task, because the calculations are restricted to finite-size clusters and thus the vectors of magnetic order are discretized. It is interesting to note that taking a pure hopping *Ansatz* within VMC, i.e. discarding the magnetic field variational parameter (cfr. Supplementary Note 5), we obtain a broad susceptibility profile with shifted peaks, which is very similar to the one provided by PFFRG. However, the corresponding variational state has a considerably higher energy. Possibly, this energy could be reduced if one were able to implement a magnetic field variational parameter for an incommensurate structure, while at the same time maintaining broad susceptibility peaks and thereby reaching better agreement with PFFRG. On the other hand, it is possible that PFFRG and VMC results will resemble each other more closely when promoting the PFFRG towards the aforementioned multi-loop scheme.

[1] A. L. Chernyshev and M. E. Zhitomirsky, Spin waves in a triangular lattice antiferromagnet: Decays, spectrum renormalization, and singularities, Phys. Rev. B **79**, 144416 (2009).

[2] A. B. Harris, C. Kallin, and A. J. Berlinsky, Possible Néel orderings of the Kagomé antiferromagnet, Phys. Rev. B **45**, 2899 (1992).

[3] J. N. Reimers and A. J. Berlinsky, Order by disorder in the classical Heisenberg kagomé antiferromagnet, Phys. Rev. B **48**, 9539 (1993).

[4] F. Wang, A. Vishwanath, and Y. B. Kim, Quantum and classical spins on the spatially distorted kagomé lattice: Applications to volborthite $Cu_3V_2O_7(OH)_2{\cdot}2H_2O$, Phys. Rev. B **76**, 094421 (2007).

[5] F. Becca and S. Sorella, *Quantum Monte Carlo Approaches for Correlated Systems* (Cambridge University Press, 2017).